Citation for published version:
Jo, WK, Kumar, S, Eslava, S & Tonda, S 2018, 'Construction of Bi_2WO_6/RGO/g-C_3N_4 2D/2D/2D hybrid Z-scheme heterojunctions with large interfacial contact area for efficient charge separation and high-performance photoreduction of CO_2 and H_2O into solar fuels', *Applied Catalysis B: Environmental*, vol. 239, pp. 586-598. https://doi.org/10.1016/j.apcatb.2018.08.056

DOI:
10.1016/j.apcatb.2018.08.056

Publication date:
2018

Document Version
Peer reviewed version

Link to publication

Publisher Rights
CC BY-NC-ND

University of Bath

General rights
Copyright and moral rights for the publications made accessible in the public portal are retained by the authors and/or other copyright owners and it is a condition of accessing publications that users recognise and abide by the legal requirements associated with these rights.

Take down policy
If you believe that this document breaches copyright please contact us providing details, and we will remove access to the work immediately and investigate your claim.

Download date: 11. Sep. 2019

Accepted Manuscript

Title: Construction of Bi_2WO_6/RGO/g-C_3N_4 2D/2D/2D hybrid Z-scheme heterojunctions with large interfacial contact area for efficient charge separation and high-performance photoreduction of CO_2 and H_2O into solar fuels

Authors: Wan-Kuen Jo, Santosh Kumar, Salvador Eslava, Surendar Tonda

PII: S0926-3373(18)30794-X
DOI: https://doi.org/10.1016/j.apcatb.2018.08.056
Reference: APCATB 16956

To appear in: *Applied Catalysis B: Environmental*

Received date: 9-6-2018
Revised date: 7-8-2018
Accepted date: 22-8-2018

Please cite this article as: Jo W-Kuen, Kumar S, Eslava S, Tonda S, Construction of Bi_2WO_6/RGO/g-C_3N_4 2D/2D/2D hybrid Z-scheme heterojunctions with large interfacial contact area for efficient charge separation and high-performance photoreduction of CO_2 and H_2O into solar fuels, *Applied Catalysis B: Environmental* (2018), https://doi.org/10.1016/j.apcatb.2018.08.056

This is a PDF file of an unedited manuscript that has been accepted for publication. As a service to our customers we are providing this early version of the manuscript. The manuscript will undergo copyediting, typesetting, and review of the resulting proof before it is published in its final form. Please note that during the production process errors may be discovered which could affect the content, and all legal disclaimers that apply to the journal pertain.

ACCEPTED MANUSCRIPT

Construction of Bi_2WO_6/RGO/g-C_3N_4 2D/2D/2D hybrid Z-scheme heterojunctions with large interfacial contact area for efficient charge separation and high-performance photoreduction of CO_2 and H_2O into solar fuels

Wan-Kuen Jo, [a] Santosh Kumar, [b] Salvador Eslava, [b] Surendar Tonda [a,*]

[a] Department of Environmental Engineering, Kyungpook National University, Daegu 702 701, South Korea.

[b] Chemical Engineering Department, University of Bath, Claverton Down, Bath, BA2 7AY, UK.

*Corresponding Author:
S. Tonda, E-mail: surendar.t86@gmail.com; surendart@knu.ac.kr
Contact No.: +82 53 950 6584.

ACCEPTED MANUSCRIPT

ACCEPTED MANUSCRIPT

Graphical abstract

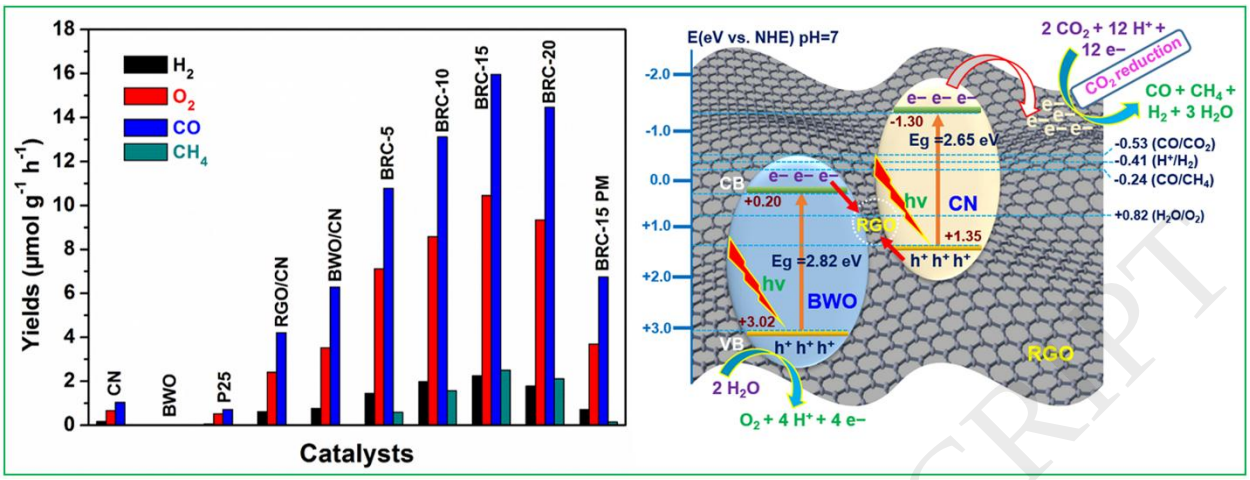

Highlights

- Bi_2WO_6/RGO/g-C_3N_4 hybrid heterojunctions with 2D/2D/2D configuration were fabricated
- Heterojunctions showed excellent CO_2 photoreduction activity to generate solar fuels
- RGO plays dual roles as a supporter and a redox mediator to promote charge separation
- Rapid charge transfer due to large interfacial contact contributed to high activity
- Hybrid heterojunctions exhibited high photostability during recycling experiments

Abstract

We have rationally constructed a hybrid heterojunction comprising of Bi_2WO_6, reduced graphene oxide, and g-C_3N_4 (BWO/RGO/CN) with a 2D/2D/2D configuration for efficient photoreduction to generate solar fuels. These heterojunctions displayed dramatically improved performance towards CO_2 reduction to generate CO and CH_4 under visible-light irradiation, compared to the base material (CN), P25 as reference, as well as binary BWO/CN and RGO/CN heterojunctions. Particularly, the BWO/RGO/CN heterojunctions with 1 wt. % RGO and 15 wt. % BWO achieved record performance in the yields of carbonaceous products

ACCEPTED MANUSCRIPT

($CO+CH_4$) compared to other synthesized catalysts, with a selectivity of 92% against H_2. The remarkable photocatalytic performance was mainly attributed to the unique 2D/2D/2D architecture that creates large interfacial contact between the constituent materials for rapid charge transfer, to hinder the direct recombination of photoinduced electrons and holes. Notably, RGO played two significant roles: as a supporter to capture the electrons from CN, and as a redox mediator to promote the Z-scheme charge transfer between CN and BWO. The result is a greater extent of charge separation in the present BWO/RGO/CN heterojunction system, as evidenced by the photoluminescence, photocurrent responses, and electron microscopy findings. More importantly, the heterojunctions displayed excellent stability during recycling tests with no obvious loss in the generation of CO and CH_4 from photoreduction of CO_2. This interesting interfacial engineering approach presented herein offers a promising route for the rational design of a new class of layered multicomponent heterojunctions with 2D/2D/2D architecture for various applications in environmental protection and solar energy conversion.

Keywords: g-C_3N_4; 2D/2D/2D architecture; Z-scheme charge transfer; hybrid heterojunction; solar energy conversion

Introduction

The substantial rise in the levels of atmospheric carbon dioxide (CO_2), considered as one of the main contributors to the greenhouse effect, has attracted significant attention in the past few decades. Meanwhile, another global issue is energy shortage prompted by the rapid depletion of fossil fuels [1-3]. As a renewable, safe, and economic technique, the photocatalytic conversion of CO_2 into sustainable feedstocks (e.g., CO, CH_4, and CH_3OH) by utilizing abundant and clean solar energy has become a promising strategy to simultaneously solve the aforementioned two problems [4-7]. Since the pioneering work in 1979 by Inoue and co-

ACCEPTED MANUSCRIPT

workers on CO_2 photoreduction in aqueous suspensions of semiconductors [8], extensive research has been directed towards designing the various catalysts to produce energy-rich compounds from photocatalytic CO_2 reduction. Nevertheless, photocatalytic CO_2 reduction is rather difficult due to its thermodynamically stable nature. Therefore, it is urgent to develop highly efficient and visible-light-active semiconductor materials in order to reduce the inert CO_2 and efficiently harness the broad solar spectrum.

Two-dimensional (2D) layered materials have gained immense attention in the area of photocatalysis in recent years [9,10]. Compared to 0D and 1D materials, these 2D materials possess impressive properties, including large specific surface area with abundant active sites, superior electron conductivity (e.g., in the case of graphene) to facilitate charge transfer and separation, and the ability to function as excellent catalyst supports (particularly nano-sized 2D materials) [11-13]. Notably, combining different 2D layered materials and constructing heterojunctions could create 2D layered composites efficient for various photocatalytic applications, due to the large contact area between the layers and the greater charge transfer rate [11]. These merits motivated us to design 2D layered composite catalysts for efficient generation of solar fuels from photocatalytic CO_2 reduction.

Recently, 2D layered graphitic carbon nitride (g-C_3N_4), which is an analogue of graphite, has been tested as an alternative to various conventional metal-containing catalysts, due to its fascinating features such as the appropriate band gap energy, tunable electronic structure, high chemical and thermal stability, elemental abundance, and eco-friendly nature [14,15]. There are many reports of applying g-C_3N_4 for decomposition of organic contaminants and hydrogen evolution from water splitting [15-18]. In contrast, its use in the photoreduction of CO_2 is scarce, partly due to the moderate photocatalytic efficiency of g-C_3N_4 owing to the fast recombination of photoexcited charge carriers. Strategies to address this limitation of g-C_3N_4 include noble metal loading, doping with metal and non-metal elements, creating textural porosity, coupling

ACCEPTED MANUSCRIPT

with conducting materials, and constructing heterojunction with other semiconductors [19-25]. Notably, the charge carrier recombination can be efficiently hindered by a charge transfer between the two semiconductors at heterojunctions, and this approach has been utilized by many researchers to develop g-C_3N_4-based composite catalysts [26].

To construct effective 2D layered composite catalysts using g-C_3N_4, it is important to combine it with another 2D semiconductor having well-matched band edge potentials. For instance, we have recently reported [27] a g-C_3N_4/NiAl-LDH hybrid heterojunction with 2D/2D configuration, which was produced by a one-step, in-situ hydrothermal route. Under visible light, this 2D/2D interface heterojunction displayed enhanced CO_2 reduction to generate CO without using a sacrificial agent, and the performance is much higher than those for NiAl-LDH and g-C_3N_4 alone. Li et al. [28] constructed a 2D/2D g-C_3N_4/Bi_2WO_6 layered composite that showed enhanced CO_2 reduction activity (compared to g-C_3N_4 and Bi_2WO_6) through Z-scheme charge transfer. Moreover, Ong and co-workers [29] reported a reduced graphene oxide (RGO)/protonated g-C_3N_4 2D/2D hybrid composite displaying enhanced CO_2 reduction activity compared to g-C_3N_4 in the presence of water vapor and light illumination. They attributed the improved CO_2 reduction performance to the rapid electron shuttling from g-C_3N_4 to RGO, which hindered the direct recombination of photoinduced electron-hole pairs. Another work by Li et al. [30] mentioned that 2D RGO improves the CO_2 photoconversion efficiency of $Fe_2V_4O_{13}$/RGO/CdS heterostructure, by playing the role of a redox mediator to promote the Z-scheme charge transfer.

Utilizing the multiple roles of 2D RGO in improving CO_2 photoreduction efficiency, and the nano-sized 2D Bi_2WO_6 sheets as catalyst support, we rationally constructed a Bi_2WO_6/RGO/g-C_3N_4 hybrid heterojunction with unique 2D/2D/2D configuration via a two-step hydrothermal route, for efficient photoreduction of CO_2 and water to solar fuels, without using a hole sacrificial agent. The synthesized heterojunctions were carefully characterized by

ACCEPTED MANUSCRIPT

different analytical techniques. Their photocatalytic performance was assessed and compared with their bare counterparts and binary heterojunctions, in not only CO_2 reduction but also water reduction to generate solar fuels under visible light. The impact of the Bi_2WO_6 content and the role of RGO on the photoreduction activities were thoroughly explored by photocurrent and photoluminescence observations. In addition, the stability of the prepared heterojunctions was assessed by carrying out four cycles of CO_2 reduction under visible-light illumination.

Experimental section

Materials

Sodium tungstate dihydrate, bismuth (III) nitrate pentahydrate, melamine, graphite powder, and triethanolamine were purchased from Sigma-Aldrich. All other chemicals used in the present work were of analytical reagent grade and used without additional treatment. The deionized water used in this work was obtained from a Wellix Plus water purification system.

Method

Synthesis of g-C_3N_4 nanosheets

Bulk g-C_3N_4 was first synthesized by directly heating the low-cost melamine in a tube furnace. In brief, 5 g of melamine powder was placed in an alumina boat with a cover, heated to 550 °C at the rate of 5 °C min^{-1} in air, and kept for 2 h. The obtained yellow aggregates were ground into fine powders for further use.

The g-C_3N_4 nanosheets were prepared via a facile heat-etching method using the bulk g-C_3N_4. Typically, 1 g of the as-obtained bulk g-C_3N_4 powder was put into an alumina dish without a cover and thermally treated at 500 °C for 2 h in a muffle furnace under static air conditions. After cooling to room temperature, a pale-yellow powder of g-C_3N_4 nanosheets was obtained and denoted as CN.

Synthesis of graphene oxide

ACCEPTED MANUSCRIPT

Graphene oxide was synthesized from graphite powder according to the modified Hummers' route [31] described as follows. Graphite powder (2 g) and $NaNO_3$ (1 g) were added into 46 mL of conc. H_2SO_4 under ice bath. Then, 6 g of $KMnO_4$ was gradually added with constant stirring, and the temperature of the mixture was maintained below 5 °C. Thereafter, the ice bath was replaced by a water bath, the suspension was heated to 35 °C, and the stirring continued for 2 h. Subsequently, 92 mL of deionized water was added dropwise, which caused the mixture to heat up to a maximum of 98 °C. The reaction mixture was maintained at that temperature for another 15 min, in order to extend the oxidation degree of the graphite oxide product. Finally, the reaction was terminated by further addition of 280 mL of deionized water followed by 20 mL of 30% H_2O_2 solution. The resultant solid product was separated by centrifugation and washed initially with aqueous HCl (5%) solution until sulfate anions were no longer detectable with $BaCl_2$. The solid was then washed repeatedly with water until the pH became neutral and finally dried in vacuum at 60 °C.

Synthesis of 2D/2D/2D BWO/RGO/CN hybrid heterojunctions

The BWO/RGO/CN 2D/2D/2D hybrid heterojunctions were prepared by a two-step hydrothermal route, which is summarized in Scheme 1. In the first step, binary RGO/CN heterojunction was prepared by a hydrothermal method described as follows. A certain amount of synthesized CN powder was first dispersed in 160 mL of water by ultrasonic treatment for 30 min. An amount of graphene oxide estimated to deposit 1 wt. % of RGO on CN was added to the suspension, which was ultrasonicated for another 30 min. After ultrasonic treatment, the suspension was agitated for 1 h at room temperature. Thereafter, the mixture was transferred into a 200-mL Teflon-lined stainless-steel autoclave and heat treated at 160 °C for 6 h. The resultant product was collected, washed, and dried at 80 °C to obtain the binary RGO/CN heterojunction. Bare RGO was also fabricated under the similar conditions but in the absence of CN powder.

ACCEPTED MANUSCRIPT

In the second step, the target BWO/RGO/CN hybrid heterojunctions were obtained by a hydrothermal method with RGO/CN heterojunction and Bi_2WO_6 precursors. In a typical experimental procedure, a calculated amount of synthesized RGO/CN heterojunction was dispersed in 160 mL of water by ultrasonication, and then 2 mmol of bismuth nitrate pentahydrate was added to the suspension and agitated for 30 min. Subsequently, 1 mmol of sodium tungstate dihydrate was added, and the mixture was agitated for another 2 h. After agitation, the uniform reaction mixture was transferred into a Teflon-lined stainless steel autoclave (200 mL), which was heat treated in an oven at 160 °C for 6 h. The resultant product was collected by centrifugation, washed repeatedly with deionized water, and dried at 80 °C overnight. In this manner, a series of BWO/RGO/CN hybrid heterojunctions were prepared with different weight percentages of BWO to RGO/CN (5, 10, 15, and 20 wt. %), and named BRC-5, BRC-10, BRC-15, and BRC-20, respectively. Bare BWO sheets were prepared via a similar process but without addition of the RGO/CN. For reference, the binary BWO/CN heterojunction (15 wt. % of BWO with respect to CN) was also synthesized by the same procedure as above, but in the presence of CN rather than RGO/CN.

The experimental details for the photocatalytic activity tests and the characterization techniques used in this study are discussed in the supplementary material.

Results and discussion

XRD analysis was applied to reveal the crystal structure and phase composition of all the prepared catalysts. In Fig. 1a, the XRD spectrum of RGO confirms the successful conversion of graphene oxide to RGO through hydrothermal treatment, and the broad diffraction peak at 25.2° corresponds to the (002) plane that is characteristic of interlayer stacking with d-spacing of 0.34 nm [32]. The XRD pattern of CN shows two distinct diffraction peaks: the stronger one at 27.56° for the (002) plane corresponds to the typical interlayer stacking of the conjugated

ACCEPTED MANUSCRIPT

aromatic segments, whereas the weak one at 13.02° for the (100) plane reflects the in-planar ordering of tri-s-triazine units [20]. The RGO/CN catalyst displays almost the same XRD pattern as that of CN but with decreased peak intensity, indicating that the integration of RGO has little impact on the CN phase structure. For BWO, the major peaks at 2θ = 28.20°, 32.76°, 47.04°, 55.82°, and 58.48° are ascribed to the crystallographic planes of (113), (200), (220), (313), and (226), respectively, which are well matched with the orthorhombic phase of Bi_2WO_6 (JCPDS No. 73−1126). Importantly, the patterns of BWO/CN and BWO/RGO/CN heterojunctions consist of diffraction peaks related to both CN and BWO. The diffraction peaks of CN cannot be discerned in the full-scale XRD spectra (Fig. 1b) due to the overlap between the primary (002) plane of CN (at 27.56°) and (113) plane of BWO (at 28.20°). However, the magnified XRD spectra (Fig. S1) clearly evidenced the overlap between these two peaks and also the slight shift of the (113) plane peak of BWO towards lower 2θ angle, which might be due to the integration between CN and BWO. As expected, the characteristic RGO peak is not observed in the BWO/CN and BWO/RGO/CN heterojunctions because of its low content. Nevertheless, the existence of RGO in these heterojunctions can be identified by UV–vis DRS, SEM, TEM, and XPS analyses, as discussed below.

UV-vis DRS analysis was conducted to explore the optical absorption characteristics of all the prepared catalysts. As can be seen in Fig. 2, CN displayed intrinsic visible light absorption with absorption edge at about 465 nm, whereas BWO exhibited an absorption edge at 440 nm. A slight blue shift in the absorption edge was noticed after the addition of BWO to either CN or RGO/CN, indicating that BWO has strong interactions with CN or RGO/CN and forms BWO/CN or BWO/RGO/CN heterojunctions. Moreover, with increase in the content of BWO on RGO/CN, the absorption edge was gradually shifted toward the lower wavelength region. Compared to CN, RGO/CN displayed a slight red-shift and distinct improvement in optical absorption over the entire wavelength region examined, indicative of the typical absorption of

ACCEPTED MANUSCRIPT

RGO [23]. More importantly, such significant enhancement in light absorption related to RGO is noticed in all the BWO/RGO/CN heterojunctions, which also provides direct and solid evidence for the presence of RGO in these heterojunctions. The enhanced visible light absorption of the BWO/RGO/CN heterojunctions can, therefore, produce more photoinduced electrons and holes needed for the photocatalytic process, which can result in extraordinary CO_2 reduction and H_2 generation activities. In addition, the band-gap energies of CN, BWO, RGO/CN, BWO/CN, and BRC-15 calculated from the DRS patterns by applying the Kubelka–Munk formula and Tauc plot were 2.65, 2.82, 2.60, 2.75, and 2.72 eV, respectively (Fig. S2).

Fig. 3 and Fig. S3 depict the FESEM images of CN, RGO, BWO, and BRC-15 samples. As can be seen in Fig. 3a, CN possesses a layered structure, which was formed by the accumulation of a few thin sheets with irregular orientation. As expected, RGO shows 2D ultrathin nanosheet structure (Fig. S3). The BWO (Fig. 3b) displays an aggregated flake-like morphology several nanometers in size. However, such aggregations of BWO are not seen in the SEM image of BRC-15 (Fig. 3c), which might be due to the fact that, during the hydrothermal treatment, several BWO sheets are grown on the surface of RGO/CN to prevent the self-aggregation of BWO in the BWO/RGO/CN heterojunctions. Magnified SEM image of BRC-15 (Fig. 3d) clearly displayed the existence of BWO, RGO, and CN in the BWO/RGO/CN heterojunctions. According to the EDS analysis (Fig. S4), the corresponding atomic ratio of C/N (36.54/41.80 = 0.87) is higher than that predicted from the stoichiometry of g-C_3N_4 (0.75), which further reveals the presence of RGO in the BRC-15 sample. Additionally, the Bi: W: O ratio in BRC-15 is 2.11:1:7.05 compared to the theoretical value of 2:1:6. The ratio of Bi to W is very close to the stoichiometry, while the excess oxygen is attributed to RGO and adsorbed water molecules as verified by XPS studies.

TEM and HRTEM analyses were employed to explore the detailed microstructure of the 2D/2D/2D BWO/RGO/CN heterojunction with reference to BWO, RGO, and CN. As shown

ACCEPTED MANUSCRIPT

in Fig. S5a, CN clearly exhibits a flat 2D layered structure composed of a few thin nanosheets, whereas RGO displays (Fig. S5b) 2D nanosheets whose ultrathin nature is indicated by the crumples. Moreover, the TEM image of BWO (Fig. S5c) also confirms the well crystallized 2D sheet-shaped morphology, and the average size of a BWO nanosheet was about 80 nm. Notably, the TEM image of BRC-15 (Fig. 4a) clearly displayed even disposition of the BWO nanosheets on the surface of RGO/CN. The magnified TEM image (Fig. 4b) further evidenced the solid interactions among BWO, RGO, and CN in the BWO/RGO/CN heterojunctions. From these results, it can be inferred that the highly-segregated BWO nanosheets in the reaction solution are strongly attached to the RGO/CN during the hydrothermal process, which leads to the formation of BWO/RGO/CN heterojunctions with highly effective 2D/2D/2D configuration. It is also worth noting from Fig. 4c that the ultrathin RGO nanosheets are strongly integrated with the CN and/or BWO, which can facilitate RGO's dual action as support material for CN and as mediator for efficient Z-scheme charge transfer between CN and BWO. Furthermore, the HRTEM image of BRC-15 (Fig. 4d) displays lattice fringes with d-spacings of 0.27 and 0.31 nm, corresponding to the (020) and (113) crystal planes of BWO, respectively [28]. The other lattice fringes spaced by 0.32 nm belong to the typical (002) planes of CN [27]. Additionally, the EDS elemental mappings of BRC-15 (Figs. 4e to j) revealed the coexistence of Bi, W, O, C, and N in the heterojunction. The uniform dispersion of these elements further confirmed the successful construction of 2D/2D/2D BWO/RGO/CN heterojunction, rather than physically mixed independent phases of BWO, RGO, and CN.

To explore the detailed surface chemical state of the elements and the interactions among BWO, RGO, and CN in the heterojunctions, XPS analysis was performed over CN, BWO, and BRC-15 catalysts. In the survey XPS spectra in Fig. 5a, the reference CN and BWO catalysts show peaks related to their respective elements, whereas the BRC-15 heterojunction exhibits peaks corresponding to Bi, W, O, C, and N elements, revealing that the heterojunction was

ACCEPTED MANUSCRIPT

comprised of CN, RGO, and BWO. The surface chemical composition of BRC-15 was estimated by XPS analysis and also compared with the EDS bulk elemental composition (Table S1). As expected, the C/N ratio (43.54/50.03 = 0.87) in BRC-15 is higher than those in CN (0.74) and the theoretical value (0.75), indicating the existence of RGO in the heterojunction, in good accordance with the EDS results (Fig. S4). Furthermore, the atomic ratio of Bi: W: O in BWO is 1.98:1:6.08, which is very close to the stoichiometric ratio of Bi_2WO_6 (2:1:6). The excess O content observed in BRC-15 was attributed to RGO and surface-adsorbed water molecules based on high-resolution O 1s spectra, as explained below.

The O 1s spectrum of BWO (Fig. 5b) can be deconvoluted into two peaks at 530.1 and 530.7 eV, which are assigned to the coordination of oxygen in Bi–O, and W–O, respectively [33]. In the O 1s spectrum of BRC-15, the two additional peaks at 532.3 and 533.8 eV correspond to C–O species of RGO and O–H groups of adsorbed water, respectively, demonstrating the interactions between BWO and RGO in the heterojunction [34-36]. For CN, the C 1s spectrum (Fig. 5c) displays two peaks positioned at 288.1 and 284.5 eV, which belong to the sp^2-hybridised C in the N-containing aromatic rings (N−C=N) and graphitic carbon or adventitious carbon (C−C) species adsorbed on the surface, respectively [37,38]. The N 1s spectrum of CN can be divided into three components at 398.3, 399.6, and 400.9 eV (Fig. 5d). The main component at 398.3 eV is ascribed to sp^2-hybridised N in triazine rings (C−N=C), and the other two components belong to bridged tertiary nitrogen $N-(C)_3$ species and amino functional groups (N−H), respectively [27,38]. Along with these three components, BRC-15 heterojunction exhibits another N component at 397.6 eV, due to pyridinic-N originating from the CN and RGO interactions [39]. The additional N 1s band in both CN and BRC-15 samples at 403.9 eV belongs to π excitations [40]. In the Bi 4f spectrum of BWO (Fig. 5e), the two bands centered at 164.2 and 158.9 eV are assigned to Bi $4f_{5/2}$ and Bi $4f_{7/2}$ of the Bi^{3+} ions, respectively [41]. The W 4f spectrum of BWO (Fig. 5f) comprises of two peaks (37.9 and 35.8

ACCEPTED MANUSCRIPT

eV) belonging to W $4f_{5/2}$ and W $4f_{7/2}$ of W^{+6}, respectively [42]. Notably, obvious increase and decrease in the respective binding energies of W 4f and N 1s were observed in BRC-15 compared to CN and BWO, and no such shift was observed for C 1s and Bi 4f bands. The shift in binding energies indicate the strong interactions and charge transfer among CN, RGO, and BWO in the BRC-15 heterojunction. Such phenomena have been reported by other research groups for various composite materials [27,43,44].

Figure 6 depicts the FT-IR spectra of the prepared BWO, CN, and BWO/RGO/CN catalysts. The spectral pattern of BWO (Fig. 6a) exhibits the typical absorption bands at 400–800 cm^{-1}, which correspond to W–O and Bi–O stretching vibrations and W–O–W bending vibrations [45,46]. For CN, various absorption peaks at 1200–1650 cm^{-1} are assigned to the typical stretching modes of C–N heterocycles [20]. The broad band of 3100–3300 cm^{-1} belongs to the stretching vibrational modes of residual uncondensed amino (N–H) fragments, and the characteristic absorption band at 806 cm^{-1} is attributed to the typical bending vibrations of s-triazine species [27]. Compared with that of CN, in BWO/RGO/CN heterojunctions the main characteristic FT-IR band at 806 cm^{-1} is shifted to lower wavenumber (Fig. 6b), indicating that the conjugated system of CN was slightly weakened and that strong interfacial interactions developed among CN, BWO, and RGO in the resulting BWO/RGO/CN catalysts [27,47].

TGA was conducted under N_2 atmosphere to verify the contents of BWO in the prepared BWO/RGO/CN heterojunctions, and the results are displayed in Fig. S6. TGA plot of BWO unveiled a total weight loss of about 2.5% in the temperature range from 25 to 800 °C, due to the elimination of surface-bound water molecules [47,48]. For CN, the weight loss region from 550 to 730 °C originates from the combustion of g-C_3N_4 [24]. The weight loss regions observed for CN and BWO could be noticed in all BWO/RGO/CN catalysts. Nevertheless, the content of BWO in the BWO/RGO/CN samples can be simply estimated from the remaining weight

ACCEPTED MANUSCRIPT

after heating to 800 °C. Thus, the weight percentages of BWO were found to be 3.2, 7.8, 12.15, and 18.21%, for BRC-5, BRC-10, BRC-15, and BRC-20, respectively.

Photocatalytic performance

The photocatalytic activities over the constructed 2D/2D/2D BWO/RGO/CN heterojunctions for CO_2 reduction were evaluated with reference to binary and pure catalysts, under visible-light using high-purity CO_2 and water vapor. Carbon monoxide was the direct and main product generated from the CO_2 photoreduction process, and H_2 and O_2 were produced from the water (vapor) reduction reaction. Besides, CH_4 was also detected as a minor carbonaceous product but only for the BWO/RGO/CN heterojunctions. In controlled experiments in the absence of catalyst or in the dark, no products (carbonaceous or not) were detected, confirming that both the catalyst and light are necessary for the photocatalytic reactions. Moreover, controlled experiments (without water vapor or with only N_2 and water vapor) further illustrated that CO and CH_4 are solely generated through the reduction of CO_2 with water vapor over the catalysts under visible light.

Figures 7a and 7b plots the evolutions of CO and CH_4 with irradiation time using different catalysts under visible light irradiation. The basic material CN showed only minimal production of CO with a total yield of 0.26 μmol for 5 h, because of the fast recombination of photoinduced electrons and holes in it. Due to its appropriate band edge positions for both water oxidation and reduction processes, CN also produced notable amounts of H_2 and O_2 by water (vapor) splitting (Figs. 7c and 7d). As expected, BWO showed negligible amounts of products from either CO_2 or water reduction, certainly due to its small conduction band (CB) potential (+0.20 eV, determined by the valence band (VB) XPS studies discussed later) that is insufficient to drive either CO_2 reduction ($E(CO_2/CO) = -0.53$ eV, and $E(CO_2/CH_4) = -0.24$ eV vs NHE at pH 7), and water reduction ($E(H^+/H_2) = -0.41$ eV vs NHE at pH 7) reactions [15]. However, the introduction of BWO on CN greatly enhanced the CO_2 reduction activity

ACCEPTED MANUSCRIPT

to reach a CO evolution rate of 1.57 μmol for 5 h. This enhanced performance of BWO/RGO might be due to the charge transfer between CN and BWO, which can suppress the recombination of photoinduced charge carriers. Meanwhile, RGO/CN also showed improved photocatalytic activity with a total CO yield of 1.05 μmol for 5 h, implying that CN hybridization with RGO has significant impact on the CO_2 photoreduction performance.

More remarkably, after introducing BWO on RGO/CN, the resulting 2D/2D/2D BWO/RGO/CN hybrid heterojunctions displayed substantially enhanced CO_2 photoreduction activities for the evolution of not only CO but also CH_4 as an additional solar fuel. As displayed in Fig. 8a, the rate of CO evolution increased with increasing BWO amount in the heterojunctions, attaining a highest CO production rate of 15.96 μmol h^{-1} g^{-1} for BRC-15 (with 1 wt. % RGO and 15 wt. % BWO), representing an outstanding 15-fold enhancement over the base material CN, and 2.5- and 3.8-fold enhancements against binary BWO/CN and RGO/CN hybrid heterojunctions, respectively. Moreover, BRC-15 showed the highest CH_4 production rate (2.51 μmol h^{-1} g^{-1}) among all BWO/RGO/CN heterojunctions, evidencing its notable selectivity of 92% for CO+CH_4 against H_2. Apart from the high CO_2 reduction activity for carbonaceous products, BRC-15 also showed obvious improvement in the production of H_2 and O_2 (Figs. 7c and 7d). Importantly, the total amount of O_2 generated on all the heterojunction catalysts was correlated with the total amount of reduction products according to the stoichiometry of the corresponding redox reactions, CH_4 ($8e^-$), O_2 ($4e^-$), H_2 ($2e^-$), and CO ($2e^-$). Nevertheless, when the BWO content in BWO/RGO/CN is increased beyond its optimum level (15 wt. %), a decline in the CO_2 reduction performance was noticed, presumably because the excess BWO may (1) cover the active sites on the surface of CN and (2) cause self-agglomeration, leading to decreased density of BWO/CN and BWO/RGO heterojunctions. Therefore, the amount of BWO is a key factor for optimizing the photocatalytic performance of BWO/RGO/CN heterojunctions.

ACCEPTED MANUSCRIPT

The effect of surface area on the photocatalytic CO_2 reduction performance of BWO/RGO/CN heterojunctions was also studied, and the results are shown in Fig. S7. The specific surface area (S_{BET}) of CN is about 96.3 m^2/g, which is far superior to that observed for BWO (18.5 m^2/g). In contrast to the CO_2 photoreduction activities, the S_{BET} of BWO/RGO/CN heterojunctions decreased gradually with increasing BWO content. However, CO_2 adsorption properties of these heterojunctions are quite different from their specific surface areas, but well consistent with the CO_2 photoreduction activity results. As shown in Fig. S8, all the BWO/RGO/CN heterojunctions displayed relatively higher CO_2 adsorption capacities than those of CN and BWO, which will be beneficial for photoreduction of CO_2. The maximum CO_2 adsorption values at atmosphere pressure and 298 K are 0.18, 0.12, and 0.23 mmol g^{-1} for CN, BWO, and BRC-15, respectively. The enhanced CO_2 adsorption on composite photocatalysts is due to the delocalized π-conjugated binding of CO_2 molecules and a large π-conjugated structure of RGO establishing the unique π−π conjugation interaction [49,50]. Therefore, enhanced CO_2 availability on photocatalyst surface significantly contribute to efficient CO_2 reduction. Besides, to investigate the role of the heterojunctions, the photocatalytic CO_2 reduction test was also carried out for a mechanical mixture of BWO, RGO (1 wt. %), and CN (15 wt. %) termed BRC-15 PM. According to the results displayed in Fig. 8a, the mechanical mixture produced much less products compared to BRC-15 as well as other BWO/RGO/CN heterojunctions constructed by two-step hydrothermal method. Hence, the loose heterojunctions in BRC-15 PM are insufficient to improve the CO_2 photoreduction activities, while the synergy among the components of the 2D/2D/2D BWO/RGO/CN hybrid heterojunctions was mainly responsible for the extraordinary photocatalytic CO_2 activities.

The performance of the present BWO/RGO/CN heterojunctions in CO_2 photoreduction was further compared with other photocatalytic systems. The first comparison was made with commercial P25 catalyst under identical experimental conditions. However, P25 exhibited

ACCEPTED MANUSCRIPT

rather poor CO_2 reduction activity (Fig. 8a) owing to its UV-only light absorption and unmatched CB potential to drive the CO_2 reduction effectively [43]. More importantly, the CO evolution over BRC-15 is also superior to various g-C_3N_4-based and other photocatalytic systems reported previously [28,51-58]. Moreover, the AQY of BRC-15 at 400 nm is 0.75%, which is also higher than the other state-of-the-art CO_2 photoreduction catalyst systems [27, 59-62].

The present 2D/2D/2D BWO/RGO/CN hybrid heterojunctions was also evaluated for H_2 evolution under visible light. No H_2 evolution was noticed in the absence of either light illumination or catalyst, indicating that H_2 is only generated from photocatalytic reaction. As displayed in Fig. S9, the amount of H_2 evolution over CN was 18.12 μmol for 4 h. After the introduction of either RGO or BWO on the surface of CN to form RGO/CN or BWO/CN, the H_2 production increased significantly. Importantly, all the 2D/2D/2D BWO/RGO/CN heterojunctions exhibited far superior photocatalytic H_2 production compared to CN, P25, RGO/CN, and BWO/CN catalysts. The highest H_2 yield (185 μmol for 4 h) was observed for BRC-15, being almost 10.2-, 3.8-, and 2.1-times superior to those for CN, RGO/CN, and BWO/CN, respectively. The general trend in H_2 evolution is similar to that for CO_2 photoreduction activities, except that BRC-20 achieved higher activity here than BRC-10. These results clearly demonstrated that the 2D/2D/2D BWO/RGO/CN hybrid heterojunctions are promising visible-light-driven catalysts for generating solar fuels from not only CO_2 reduction but also water splitting.

To investigate the stability and recycling capability of the BWO/RGO/CN heterojunctions, four successive experimental runs were conducted using BRC-15 as a representative for the reduction of CO_2 to CO and CH_4. As can be seen in Fig. 8b, BRC-15 retains its notable activity after four cycles under identical conditions with no significant deactivation toward CO and CH_4 evolution. Moreover, XRD and FT-IR analyses (Figs. S10a and S10b) clearly confirmed

ACCEPTED MANUSCRIPT

that the phase and chemical structures of BRC-15 did not change significantly during the prolonged reaction. Based on these experimental outcomes, it can be concluded that the constructed 2D/2D/2D BWO/RGO/CN heterojunctions are highly stable candidates for practical application in generating solar fuels.

Photocatalytic mechanism

The remarkably high photocatalytic performance of the BWO/RGO/CN heterojunctions can be primarily ascribed to their notable 2D/2D/2D configuration, together with other favorable characteristics. In general, the strong optical absorption, high specific surface area, and rapid separation and transfer efficiency of photoinduced charge carriers help to improve the catalytic activity. Nevertheless, in the present case, the specific surface area is ruled out as a factor since it does not affect the CO_2 photoreduction of BWO/RGO/CN heterojunctions as discussed earlier. The DRS results reveal that introducing RGO on CN remarkably improves the optical absorption, whereas no obvious change in light absorption was observed after adding BWO. Although the final BWO/RGO/CN heterojunctions possess strong light absorption in the visible region, this alone cannot account for their remarkable photocatalytic performance.

In order to explain how the interfacial charge transfer among RGO, BWO, and CN leads to the remarkable photocatalytic performance of the BWO/RGO/CN heterojunction system, PL spectral studies were conducted. As is well known, the intensity of the PL emission peak is positively correlated with the recombination probability of the photoexcited charge carriers [63]. Figure 9a displays the PL spectra of CN, RGO/CN, BWO/CN, and BWO/RGO/CN catalysts. CN showed the strongest PL emission band at 460 nm, which indicates the rapid charge recombination in it. The addition of RGO on CN appreciably diminished the PL emission intensity due to strong electron shuttling from CN to RGO at their interface, hindering the direct recombination of charge carriers. It is clear in Fig. 9a that BWO/CN displayed an appreciable decrease in the PL emission intensity compared to CN, perhaps due to charge

ACCEPTED MANUSCRIPT

transfer between CN and BWO through Z-scheme, which facilitates the separation of charge carriers. Compared to CN and binary catalysts of RGO/CN and BWO/CN, a substantial quenching in PL emission intensity was observed for the BWO/RGO/CN heterojunctions, and the trend in PL quenching was in good agreement with the photocatalytic activity results. This drastic depletion of PL emission signals in the BWO/RGO/CN heterojunctions perhaps originated from the joint promotion of charge transfer by RGO and BWO, as mentioned above. Besides, the TEM and XPS results also show that RGO has strong interactions with both CN and BWO, which can, therefore, justify its dual action as a supporter to capture the electrons from CN and as a redox mediator to promote the Z-scheme charge transfer between CN and BWO. In addition, the relatively higher PL emission signal of BRC-20 compared to BRC-15 further elucidates the effect of BWO content in the BWO/RGO/CN heterojunctions in facilitating charge separation.

Furthermore, time-resolved PL studies were applied to better understand the roles of interface on the dynamics of the photoinduced charge carriers. In Fig. 9b, a "biexponential" function was used to fit the decay curves as follows [41].

$$Fit = A + B_1 e^{\left(\frac{-t}{\tau_1}\right)} + B_2 e^{\left(\frac{-t}{\tau_2}\right)}$$

Where A is an exponential constant and *t* is time. The shorter decay lifetime (τ_1) is attributed to the non-radiative relaxation process, and the longer decay lifetime (τ_1) comes from the radiative process which is related to the direct recombination of photoinduced charge carriers. B_1 and B_2 are constants related to non-radiative and radiative relaxation processes, respectively. The average charge carrier lifetime (τ) was estimated from the equation as follows:

$$\tau = \frac{B_1\tau_1^2 + B_2\tau_2^2}{B_1\tau_1 + B_2\tau_2}$$

Table S2 lists the fitted parameters of the time-resolved PL decay spectra of CN, RGO/CN, BWO/CN, and BRC-15. The parameter (χ^2) indicates the goodness of fit, and it is close to 1 for

ACCEPTED MANUSCRIPT

all four catalysts. BRC-15 showed a charge carrier lifetime of 10.07 ns, which is clearly higher than RGO/CN (4.80 ns) and BWO/CN (5.93 ns), and much higher than CN (2.52 ns). This shows that the formation of large intimate interfaces in the BWO/RGO/CN heterojunctions slows down the charge carrier recombination, owing to the electric field associated with the heterojunction. In particular, the electrons and holes were separated by the Z-scheme, which resulted in decreased PL intensity and increased lifetime of charge carriers in the BWO/RGO/CN heterojunctions. Combined with the UV-vis DRS, XPS, and FT-IR findings, the PL results further evidenced the formation of strong interface heterojunction with Z-scheme separation, which could contribute to the suppression of charge recombination and efficient charge transfer. As a result, higher activities in the CO_2 and water photoreduction were achieved.

To give additional evidence to the exceptional charge separation in the BWO/RGO/CN heterojunctions, transient photocurrent analysis was carried out. Figure 10 depicts the photocurrent responses of the BWO/RGO/CN heterojunctions using CN, BWO, RGO/CN, and BWO/CN as references, during five on-off cycles of intermittent light illumination. All the catalysts displayed prompt and reproducible photocurrent responses for each irradiation period, and the photocurrent dropped instantly in the dark and recovered once the light was on. Notably, all the BWO/RGO/CN heterojunctions displayed better photocurrent responses than those of CN, BWO, and binary (BWO/CN and RGO/CN) catalysts. Hence, there is greater separation of the photoinduced charge carriers in BWO/RGO/CN heterojunctions, a result of their exceptional 2D/2D/2D configuration that facilitates intimate interfacial contact among the constituent BWO, RGO, and CN. Moreover, compared to BWO/CN, BRC-15 exhibited strong photocurrent response under visible light, further proving our assumption about the dual roles of RGO in the BWO/RGO/CN heterojunctions, namely as a redox mediator and as a supporter

ACCEPTED MANUSCRIPT

to facilitate charge separation. These results are well consistent with the PL and photocatalytic results.

Thus, the photocurrent response and PL experimental data constitute sufficient evidence for the dual function of RGO and the intimate interfacial contact among BWO, RGO, and CN owing to the 2D/2D/2D configuration, where the photoexcited charge carriers could be efficiently separated. This explains the extraordinary photocatalytic performance of the BWO/RGO/CN heterojunctions.

It is generally accepted that charge separation in composite catalysts is associated with the band alignment-prompted charge transfer at the interfaces of the constituent materials [27, 63,64]. In this work, VB-XPS analysis was conducted to determine the band edge positions of CN and BWO, and the results are displayed in Fig. 11. The VB edge potentials of CN and BWO were estimated to be approximately +1.35 and +3.02 eV, respectively, which are in good accordance with previous reports [27,36]. The CB edge potentials calculated from the band-gap energies of CN (2.65 eV) and BWO (2.82 eV) were -1.30 and +0.20 eV, respectively. To further verify these band-edge potentials of CN and BWO, Mott-Schottky measurements were conducted (Fig. S11). The slopes of the curves are positive for both CN and BWO, indicating their n-type semiconductor nature [65]. From the Mott–Schottky plots, the flat-band potentials were estimated to be −1.28 and +0.19 eV (vs NHE at pH 7) for CN and BWO, respectively. In n-type semiconductors, the flat-band potential is an approximation of the potential of the CB [66]. Therefore, the CB potentials of CN and BWO obtained from the Mott-Schottky measurements are well consistent with the estimated CB values from VB-XPS analysis. Based on the results from VB-XPS and Mott-Schottky plots, the CB potential of CN is clearly more negative than the CB of BWO, whereas the VB of CN is less positive than the VB for BWO. Nevertheless, the transfer directions of the photoexcited electrons and holes in the system remain unclear, since both double-transfer and Z-scheme transfer modes are possible for the

ACCEPTED MANUSCRIPT

above-mentioned band edge positions. In previous reports [28,36,45,67], both transfer modes have been proposed for the g-C_3N_4/Bi_2WO_6 system in various photocatalytic applications. For the present BWO/RGO/CN heterojunctions, in the double-transfer mode the photoreduction process would proceed on the CB of BWO, and photooxidation reaction on the VB of CN. This can be verified by measuring the production rate of hydroxyl radicals (•OH) using the terephthalic acid PL probing technique. As expected, CN showed poor PL emission intensities (Fig. S12a), because of the VB potential of CN is much lower than the standard oxidation potential of HO^-/•OH (+2.4 eV vs NHE) [68,69]. As shown in Fig. S12b, a significant increase in the PL emission intensity with increasing irradiation time was observed, clearly demonstrating that •OH were generated on the surface of the BRC-15 catalyst. Considering the VB potentials of both CN (+1.35 eV) and BWO (+3.02 eV), only the photoinduced holes from the VB of BWO are able to directly produce •OH. Therefore, this double-transfer mode does not work in the present heterojunction system. Moreover, according to the photocatalytic activity results, this double-transfer mechanism is impossible since the CB potential of BWO (+0.20 V) is not sufficient to drive either CO_2 or water reduction reactions.

Based on the above findings and the remarkable performance of the BWO/RGO/CN heterojunctions for CO_2 reduction and H_2 generation, an RGO-mediated Z-scheme charge transfer mechanism is proposed. As illustrated in Fig. 12, both CN and BWO are excited to generate electrons and holes under visible light, owing to their suitable band-gap energies for absorbing visible light. Due to the intimate interfaces existing among BWO, RGO, and CN, the generated electrons in the CB of BWO quickly transfer to the VB of CN through RGO redox mediator to combine with holes in the VB of CN, resulting in the accumulation of holes in the VB of BWO and electrons in the CB of CN. In such a way, CN and BWO are mutually activated as manifested by the efficient charge carrier separation. The accumulated electrons in the CB of CN further transfer to the RGO through a percolation mechanism, due to the

ACCEPTED MANUSCRIPT

exceptional storage capacity and electron conductivity of RGO [29,70]. Meanwhile, the gathered holes in the VB of BWO can oxidize the chemisorbed water molecules to produce O_2 and protons. Due to their delocalized π-conjugated binding II_3, CO_2 molecules can easily adsorb onto the surface of RGO through π-π conjugation interactions and become destabilized (i.e. activated) [23,71]. The assembled electrons on the surface of RGO can easily reduce these activated CO_2 molecules to produce $CO_2^{\bullet-}$ radicals, which subsequently generate CO, CH_4, and H_2 with the assistance of protons. It is well known that the formation of CO from CO_2 photoreduction is thermodynamically more favored compared to the formation of CH_4, because the former needs only $2e^-/2H^+$ whereas the latter requires $8e^-/8H^+$. This is the reason why only CO and H_2 were generated by the CN, RGO/CN, and BWO/CN catalysts. In contrast, introducing both RGO and BWO on the CN substantially decreases the direct recombination of photoinduced electrons and holes, resulting in increased electron density on the surface of RGO. As a result, CH_4 is evolved in addition to CO on the BWO/RGO/CN heterojunctions. In the case of H_2 generation, the enriched electrons on the RGO surface effectively generate H_2, and holes on the VB of BWO can react with triethanolamine (TEOA) to suppress the charge recombination. The main steps involved in the CO_2 photoreduction and H_2 evolution processes are summarized by the following equations.

$$\mathrm{BWO/RGO/CN} + h\nu \longrightarrow \mathrm{BWO/RGO/CN}\ (h_{VB}^{+} + e_{CB}^{-})$$

$$\mathrm{BWO/RGO/CN}\ (h_{VB}^{+} + e_{CB}^{-}) \longrightarrow \mathrm{RGO}\ (e^{-}) + \mathrm{BWO}\ (h_{VB}^{+})$$

$$\mathrm{BWO}\ (h_{VB}^{+}) + 2H_2O \longrightarrow O_2 + 4H^{+} + 4e^{-};\ E^0 = +0.82\ \mathrm{V}$$

$$\mathrm{RGO}\ (8e^{-}) + 8H^{+} + CO_2 \longrightarrow \mathrm{RGO} + CH_4 + 2H_2O;\ E^0 = -0.24\ \mathrm{V}$$

$$\mathrm{RGO}\ (2e^{-}) + 2H^{+} + CO_2 \longrightarrow \mathrm{RGO} + CO + H_2O;\ E^0 = -0.53\ \mathrm{V}$$

$$\mathrm{RGO}\ (2e^{-}) + 2H^{+} \longrightarrow \mathrm{RGO} + H_2;\ E^0 = -0.41\ \mathrm{V}$$

ACCEPTED MANUSCRIPT

$$\mathrm{BWO}\ (h^{+}_{VB}) + \mathrm{TEOA} \longrightarrow \mathrm{BWO} + \mathrm{TEOA}^{+}$$

Conclusions

In summary, BWO/RGO/CN hybrid heterojunctions with 2D/2D/2D configuration were successfully fabricated by a two-step hydrothermal route. The 2D/2D/2D architecture was confirmed to have large interfaces between the constituent materials. Notably, upon visible light irradiation, the BWO/RGO/CN heterojunctions exhibited excellent performance for the evolution of CO and CH_4 from CO_2 reduction and H_2 evolution from water reduction, compared to the CN, BWO, P25, and binary BWO/CN and RGO/CN catalysts. More interestingly, an efficient Z-scheme charge separation and transfer mechanism was proposed where RGO plays dual roles as a supporter and a redox mediator for the high photocatalytic performance of the BWO/RGO/CN heterojunctions. With their high stability in repeated catalytic cycles, the present 2D/2D/2D BWO/RGO/CN heterojunctions are promising candidate photocatalysts for the practical generation of solar fuels.

Acknowledgments

This work was supported by the National Research Foundation of Korea grant funded by the Korea government (MSIP) (No. 2016R1A2B4009122 and No. 2017R1A4A1015628). SK thanks the Engineering and Physical Sciences Research Council (EPSRC) (EP/R026041/1) for financial support.

References

[1] M.R. Hoffmann, S.T. Martin, W. Choi, D.W. Bahnemann, Chem. Rev. 95 (1995) 69–96.

[2] K. Rajeshwar, M.E. Osugi, W. Chanmanee, C.R. Chenthamarakshan, M.V.B. Zanoni, P. Kajitvichyanukul, R. Krishnan-Ayer, J. Photochem. Photobiol. C: Photochem. Rev. 9 (2008) 171–192.

[3] P.D. Tran, L.H. Wong, J. Barber, J.S.C. Loo, Energy Environ. Sci. 5 (2012) 5902–5918.

ACCEPTED MANUSCRIPT

[4] A. Kubacka, M. Fernandez-García, G. Colon, Chem. Rev. 112 (2012) 1555−1614.

[5] D.D. Zhu, J.L. Liu, S.Z. Qiao, Adv. Mater. 28 (2016) 3423−3452.

[6] E.V. Kondratenko, G. Mul, J. Baltrusaitis, G.O. Larrazabal, J. Perez-Ramírez, Energy Environ. Sci. 6 (2013) 3112−3135.

[7] J.L. White, M.F. Baruch, J.E. Pander III, Y. Hu, I.C. Fortmeyer, J.E. Park, T. Zhang, K. Liao, J. Gu, Y. Yan, T.W. Shaw, E. Abelev, A.B. Bocarsly, Chem. Rev. 115 (2015) 12888–12935.

[8] T. Inoue, A. Fujishima, S. Konishi, K. Honda, Nature 277 (1979) 637−638.

[9] B. Luo, G. Liu, L. Wang, Nanoscale 8 (2016) 6904–6920.

[10] S. Ida, T. Ishihara, J. Phys. Chem. Lett. 5 (2014) 2533–2542.

[11] J. Low, S. Cao, J. Yu, S. Wageh, Chem. Commun. 50 (2014) 10768−10777.

[12] Y.T. Liang, B.K. Vijayan, O. Lyandres, K.A. Gray, M.C. Hersam, J. Phys. Chem. Lett. 3 (2012) 1760−1765.

[13] J. Low, B. Cheng, J. Yu, M. Jaroniec, Energy Storage Mater. 3 (2016) 24−35.

[14] X.C. Wang, K. Maeda, A. Thomas, K. Takanabe, G. Xin, J.M. Carlsson, K. Domen, M. Antonietti, Nat. Mater. 8 (2009) 76−80.

[15] W.J. Ong, L.L Tan, Y.H. Ng, S.T. Yong, S.P. Chai, Chem. Rev. 116 (2016) 7159–7329.

[16] S. Cao, J. Low, J. Yu, M. Jaroniec, Adv. Mater. 27 (2015) 2150−2176.

[17] S. Ye, R. Wang, M.Z. Wu, Y.P. Yuan, Appl. Surf. Sci. 358 (2015) 15−27.

[18] D. Xia, W. Xu, L. Hu, C. He, D.Y.C. Leung, W. Wang, P.K. Wong, J. Hazard. Mater. 349 (2018) 91–100.

[19] J. Xue, S. Ma, Y. Zhou, Z. Zhang, M. He, ACS Appl. Mater. Interfaces 7 (2015) 9630–9637.

[20] S. Tonda, S. Kumar, S. Kandula, V. Shanker, J. Mater. Chem. A 2 (2014) 6772–6780.

ACCEPTED MANUSCRIPT

[21] L. Zhou, H. Zhang, H. Sun, S. Liu, M.O. Tade, S. Wang, W. Jin, Catal. Sci. Technol. 6 (2016) 7002−7023.

[22] H. Huang, K. Xiao, N. Tian, F. Dong, T. Zhang, X. Du, Y. Zhang, J. Mater. Chem. A 5 (2017) 17452−17463.

[23] W.J. Ong, L.L. Tan, S.P. Chai, S.T. Yong, Chem. Commun. 51 (2015) 858−861.

[24] S. Kumar, S. Tonda, A. Baruah, V. Shanker, J. Mater. Chem. A 1 (2013) 5333–5340.

[25] R. Wang, T. Yan, L. Han, G. Chen, H. Li, J. Zhang, L. Shi, D. Zhang, J. Mater. Chem. A 6 (2018) 5752–5761.

[26] Z. Zhao, Y. Sun, F. Dong, Nanoscale 7 (2015) 15–37.

[27] S. Tonda, S. Kumar, M. Bhardwaj, P. Yadav, S.B. Ogale, ACS Appl. Mater. Interfaces 10 (2018) 2667–2678.

[28] M. Li, L. Zhang, X. Fan, Y. Zhou, M. Wu, J. Shi, J. Mater. Chem. A 3 (2015) 5189–5196.

[29] W.J. Ong, L.L. Tan, S.P. Chai, S.T. Yong, A.R. Mohamed, Nano Energy 13 (2015) 757–770.

[30] P. Li, Y. Zhou, H. Li, Q. Xu, X. Meng, X. Wang, M. Xiao, Z. Zou, Chem. Commun. 51 (2015) 800–803.

[31] W.S. Hummers, R.J. Offeman, J. Am. Chem. Soc. 80 (1958) 1339–1339.

[32] W. Fan, Q. Lai, Q. Zhang, Y. Wang, J. Phys. Chem. C 115 (2011) 10694–10701.

[33] Y. Lv, W. Yao, R. Zong, Y. Zhu, Sci. Rep. 6 (2016) 19347.

[34] C. Wang, D. Meng, J. Sun, J. Memon, Y. Huang, J. Geng, Adv. Mater. Interfaces 1 (2014) 1300150.

[35] M. Gopiraman, H. Bang, S.G. Babu, K. Wei, R. Karvembu, I.S. Kim, Catal. Sci. Technol. 4 (2014) 2099–2106.

[36] D. Ma, J. Wu, M. Gao, Y. Xin, T. Ma, Y. Sun, Chem. Eng. J. 290 (2016) 136–146.

ACCEPTED MANUSCRIPT

[37] J. Wang, L. Tang, G. Zeng, Y. Deng, Y. Liu, L. Wang, Y. Zhou, Z. Guo, J. Wang, C. Zhang, Appl. Catal. B Environ. 209 (2017) 285–294.

[38] S. Tonda, S. Kumar, Y. Gawli, M. Bhardwaj, S.B. Ogale, Int. J. Hydrogen Energy 42 (2017) 5971–5984.

[39] Q. Liu, J. Zhang, Langmuir 29 (2013) 3821–3828.

[40] Y. Liao, S. Zhu, J. Ma, Z. Sun, C. Yin, C. Zhu, X. Lou, D. Zhang, ChemCatChem 6 (2014) 3419–3425.

[41] J. Wang, L. Tang, G. Zeng, Y. Liu, Y. Zhou, Y. Deng, J. Wang, B. Peng, ACS Sustainable Chem. Eng. 5 (2017) 1062−1072.

[42] Z.S. Seddigi, M.A. Gondal, S.G. Rashid, M.A. Abdulaziz, S.A. Ahmed, J. Mol. Catal. A Chem. 420 (2016) 167–177.

[43] S. Kumar, M.A. Isaacs, R. Trofimovaite, C.M.A. Parlett, R.E. Douthwaite, B. Coulson, M.C.R. Cockett, K. Wilson, A.F. Lee, Appl. Catal. B Environ. 209 (2017) 394−404.

[44] Y. Dou, S. Zhang, T. Pan, S. Xu, A. Zhou, M. Pu, H. Yan, J. Han, M. Wei, D.G. Evans, X. Duan, Adv. Funct. Mater. 25 (2015) 2243–2249.

[45] Y. Tian, B. Chang, J. Lu, J. Fu, F. Xi, X. Dong, ACS Appl. Mater. Interfaces 5 (2013) 7079−7085.

[46] J. Yu, J. Xiong, B. Cheng, Y. Yu, J. Wang, J. Solid State Chem. 178 (2005) 1968−1972.

[47] Y. Wang, X. Bai, C. Pan, J. He, Y. Zhu, J. Mater. Chem. 22 (2012) 11568–11573.

[48] S.H. Chen, Z. Yin, S.L. Luo, X.J. Li, L.X. Yang, F. Deng, Appl. Surf. Sci. 259 (2012) 7–12.

[49] J. Low, J. Yu, W. Ho, J. Phys. Chem. Lett. 6 (2015) 4244−4251.

[50] D. Xu, B. Cheng, W. Wang, C. Jiang, J. Yu, Appl. Catal. B Environ. 231 (2018) 368–380.

ACCEPTED MANUSCRIPT

[51] J.C. Wang, H.C. Yao, Z.Y. Fan, L. Zhang, J.S. Wang, S.Q. Zang, Z.J. Li, ACS Appl. Mater. Interfaces 8 (2016) 3765−3775.

[52] Y. Wang, X. Bai, H. Qin, F. Wang, Y. Li, X. Li, S. Kang, Y. Zuo, L. Cui, ACS Appl. Mater. Interfaces 8 (2016) 17212−17219.

[53] Y. Bai, T. Chen, P. Wang, L. Wang, L. Ye, X. Shi, W. Bai, Sol. Energy Mater. Sol. Cells 157 (2016) 406−414.

[54] S. Zhou, Y. Liu, J. Li, Y. Wang, G. Jiang, Z. Zhao, D. Wang, A. Duan, J. Liu, Y. Wei, Appl. Catal. B Environ. 158–159 (2014) 20–29.

[55] M. Li, L. Zhang, M. Wu, Y. Du, X. Fan, M. Wang, L. Zhang, Q. Kong, J. Shi, Nano Energy 19 (2016) 145–155.

[56] H. Zhou, J. Guo, P. Li, T. Fan, D. Zhang, J. Ye, Sci. Rep. 3 (2013) 1667.

[57] S. Liu, B. Weng, Z.R. Tang, Y.J. Xu, Nanoscale 7 (2015) 861−866.

[58] C. Wang, R.L. Thompson, P. Ohodnicki, J. Baltrus, C. Matranga, J. Mater. Chem. 21 (2011) 13452−13457.

[59] M.F. Kuehnel, K.L. Orchard, K.E. Dalle, E. Reisner, J. Am. Chem. Soc. 139 (2017) 7217−7223.

[60] X. An, K. Li, J. Tang, ChemSusChem 7 (2014) 1086−1093.

[61] K. Wada, C.S.K. Ranasinghe, R. Kuriki, A. Yamakata, O. Ishitani, K. Maeda, ACS Appl. Mater. Interfaces 9 (2017) 23869–23877.

[62] L. Ye, X. Jin, C. Liu, C. Ding, H. Xie, K.H. Chu, P.K. Wong, Appl. Catal. B Environ. 187 (2016) 281−290.

[63] W.K. Jo, Y.G. Kim, S. Tonda, J. Hazard. Mater. 357 (2018) 19–29.

[64] W.K. Jo, S. Kumar, P. Yadav, S. Tonda, Appl. Surf. Sci. 445 (2018) 555–562.

[65] L. Li, J. Yan, T. Wang, Z.J. Zhao, J. Zhang, J. Gong, N. Guan, Nat. Commun. 6, (2015) 5881–5891.

ACCEPTED MANUSCRIPT

[66] J. Xiao, Y. Xie, F. Nawaz, S. Jin, F. Duan, M. Li, H. Cao, Appl. Catal. B Environ. 181 (2016) 420–428.

[67] X. Xiao, J. Wei, Y. Yang, R. Xiong, C. Pan, J. Shi, ACS Sustainable Chem. Eng. 4 (2016) 3017−3023.

[68] Z. Huang, Q. Sun, K. Lv, Z. Zhang, M. Li, B. Li, Appl. Catal. B Environ. 164 (2015) 420–427.

[69] Y. Li, K. Lv, W. Ho, F. Dong, X. Wu, Y. Xia, Appl. Catal. B Environ. 202 (2017) 611–619.

[70] Y. Hou, Z. Wen, S. Cui, X. Guo, J. Chen, Adv. Mater. 25 (2013) 6291–6297.

[71] J. Yu, J. Jin, B. Cheng, M. Jaroniec, J. Mater. Chem. A 2 (2014) 3407–3416.

ACCEPTED MANUSCRIPT

ACCEPTED MANUSCRIPT

Figure captions

Scheme 1. Schematic diagram for the synthesis process of BWO/RGO/CN 2D/2D/2D hybrid heterojunctions by a two-step hydrothermal route.

Fig. 1. (a, b) XRD patterns of the prepared RGO, CN, BWO, BWO/CN, RGO/CN, and BWO/RGO/CN catalysts.

Fig. 2. UV-vis DRS patterns of all the prepared samples.

Fig. 3. SEM images of (a) CN, (b) BWO, and (c, d) BRC-15 samples.

Fig. 4. (a, b) TEM and (c, d) HR-TEM images of the BRC-15 heterojunction sample. (e to j) EDS elemental mappings of its constituent elements.

Fig. 5. XPS profiles of CN, BWO, and BRC-15 catalysts. (a) Survey spectral patterns, (b) O 1s, (c) C 1s, (d) N 1s, (e) Bi 4f, and (f) W 4f spectra.

Fig. 6. (a) FT-IR and (b) magnified FT-IR profiles of the prepared CN, BWO, and BWO/RGO/CN heterojunction catalysts.

Fig. 7. Time-dependent (a) CO, (b) CH_4, (c) H_2, and (d) O_2 amounts generated over all the synthesized photocatalysts (conditions: 300 W xenon lamp with a UV cut-off filter ($\lambda \geq 420$ nm) as light source and 50 mg catalyst).

Fig. 8. (a) Comparison of the photocatalytic CO, CH_4, H_2, and O_2 production rates of all the synthesized photocatalysts under visible light illumination for 5h. (b) Reusability of the optimum BRC-15 catalyst for evolving CO and CH_4 from CO_2 photoreduction over four successive experimental runs.

Fig. 9. (a) Steady-state PL spectra of CN, BWO/CN, RGO/CN, and BWO/RGO/CN catalysts. (b) Time-resolved PL profiles of CN, BWO/CN, RGO/CN, and BRC-15 catalysts.

Fig. 10. Photocurrent responses of CN, BWO, BWO/CN, RGO/CN, and BWO/RGO/CN heterojunction catalysts.

Fig. 11. Valance band XPS profiles of CN and BWO catalysts.

ACCEPTED MANUSCRIPT

Fig. 12. Schematic illustration of the proposed mechanism for CO_2 photoreduction in the BWO/RGO/CN 2D/2D/2D hybrid heterojunctions.

ACCEPTED MANUSCRIPT

ACCEPTED MANUSCRIPT

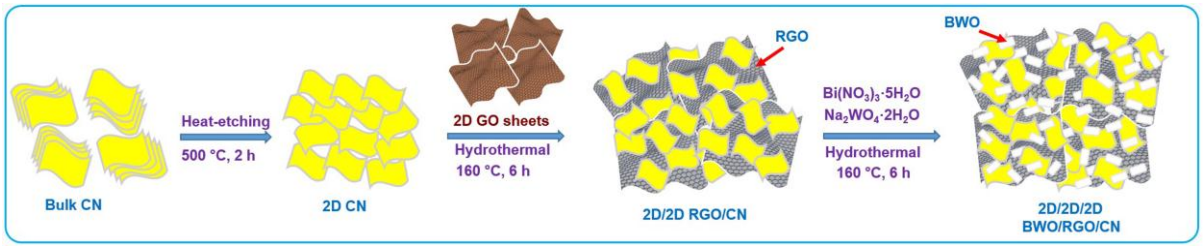

Scheme 1. Schematic diagram for the synthesis process of BWO/RGO/CN 2D/2D/2D hybrid heterojunctions by a two-step hydrothermal route.

ACCEPTED MANUSCRIPT

ACCEPTED MANUSCRIPT

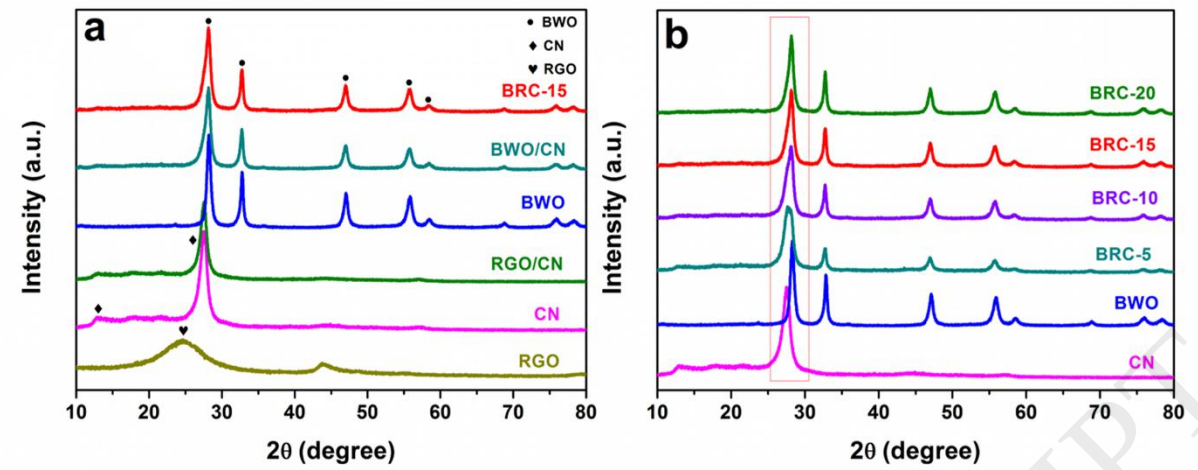

Fig. 1. (a, b) XRD patterns of the prepared RGO, CN, BWO, BWO/CN, RGO/CN, and BWO/RGO/CN catalysts.

ACCEPTED MANUSCRIPT

ACCEPTED MANUSCRIPT

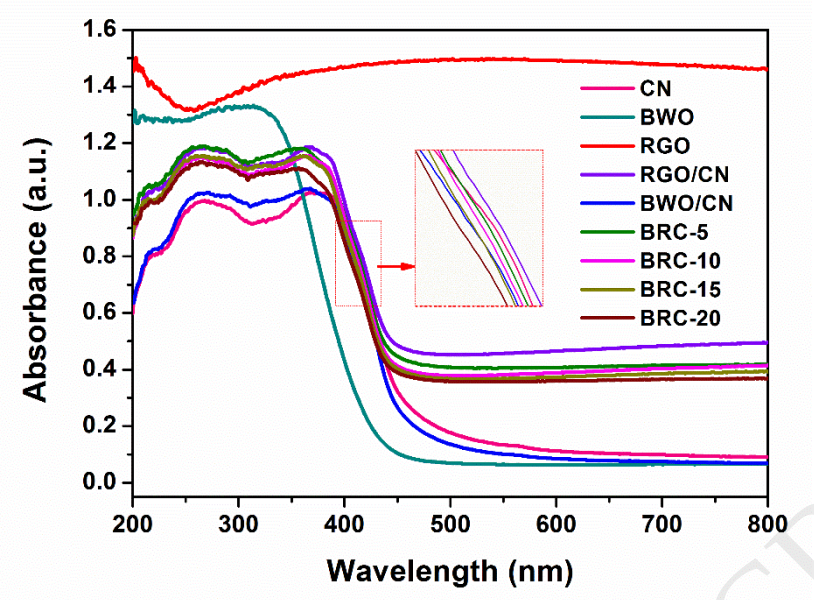

Fig. 2. UV-vis DRS patterns of all the prepared samples.

ACCEPTED MANUSCRIPT

ACCEPTED MANUSCRIPT

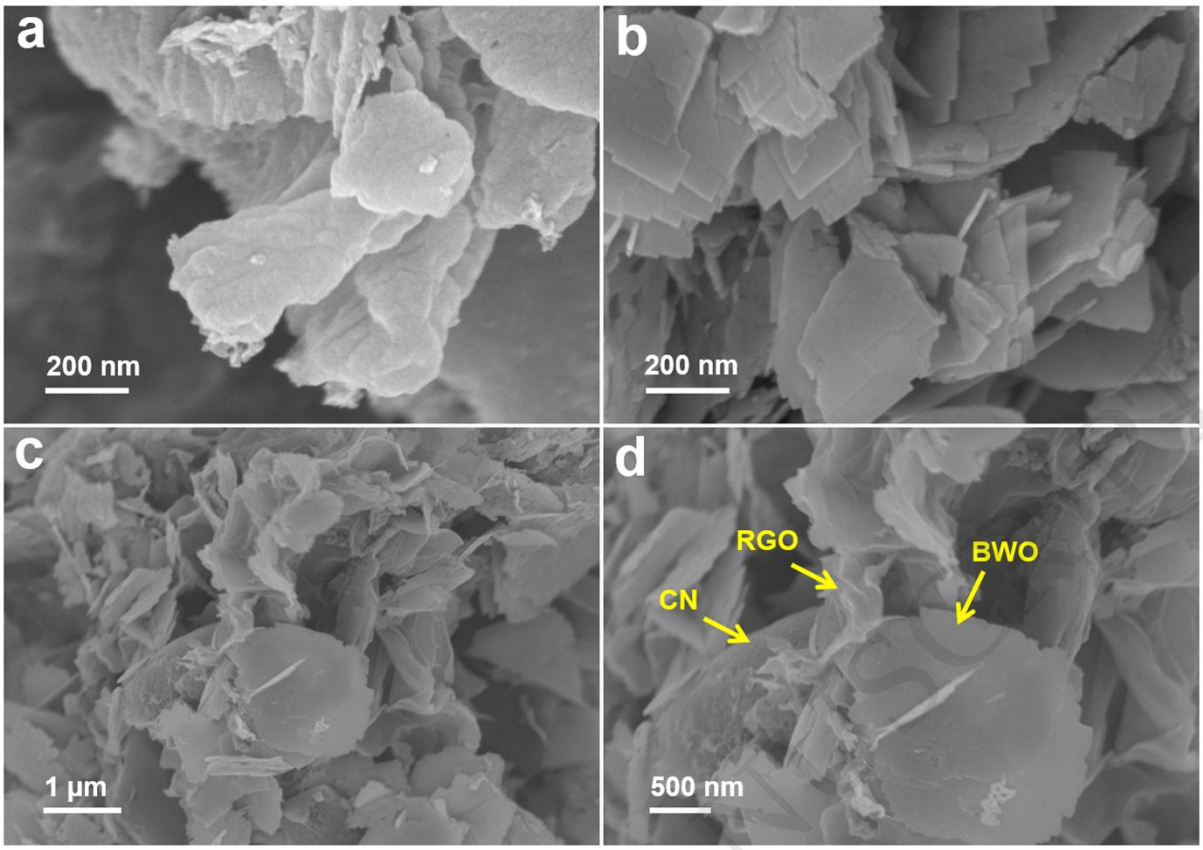

Fig. 3. SEM images of (a) CN, (b) BWO, and (c, d) BRC-15 samples.

ACCEPTED MANUSCRIPT

ACCEPTED MANUSCRIPT

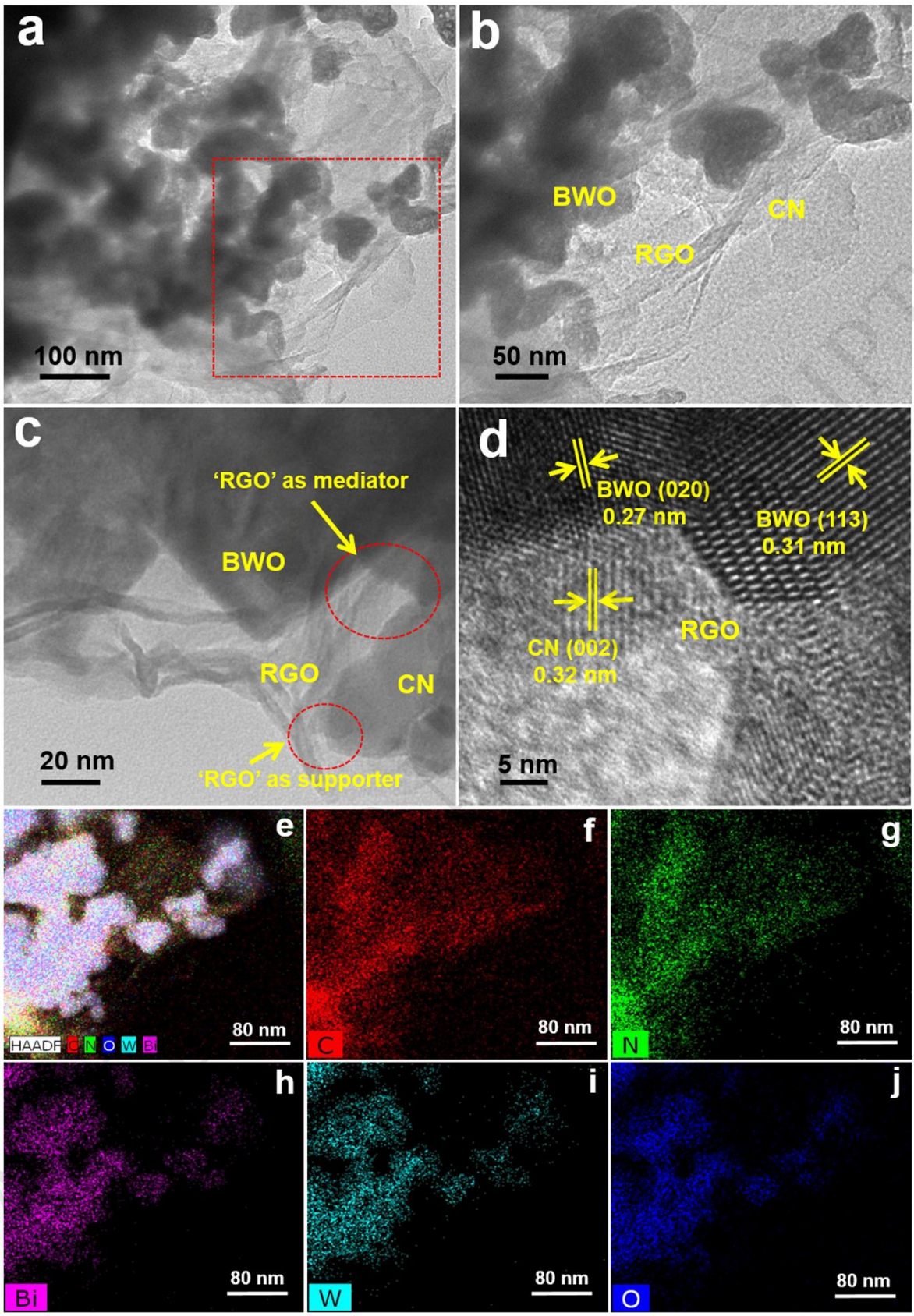

Fig. 4. (a, b) TEM and (c, d) HR-TEM images of the BRC-15 heterojunction sample. (e to j) EDS elemental mappings of its constituent elements.

ACCEPTED MANUSCRIPT

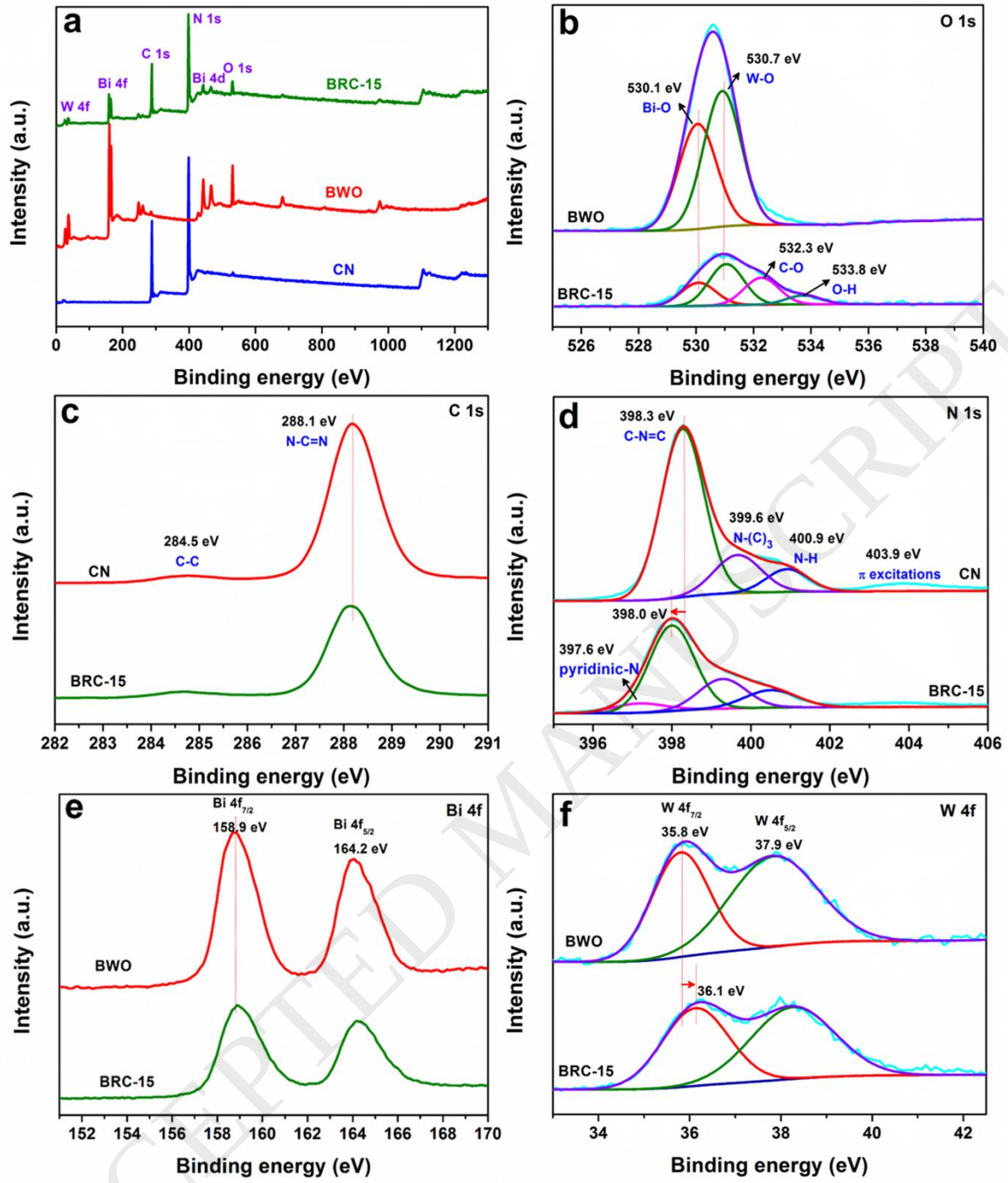

Fig. 5. XPS profiles of CN, BWO, and BRC-15 catalysts. (a) Survey spectral patterns, (b) O 1s, (c) C 1s, (d) N 1s, (e) Bi 4f, and (f) W 4f spectra.

ACCEPTED MANUSCRIPT

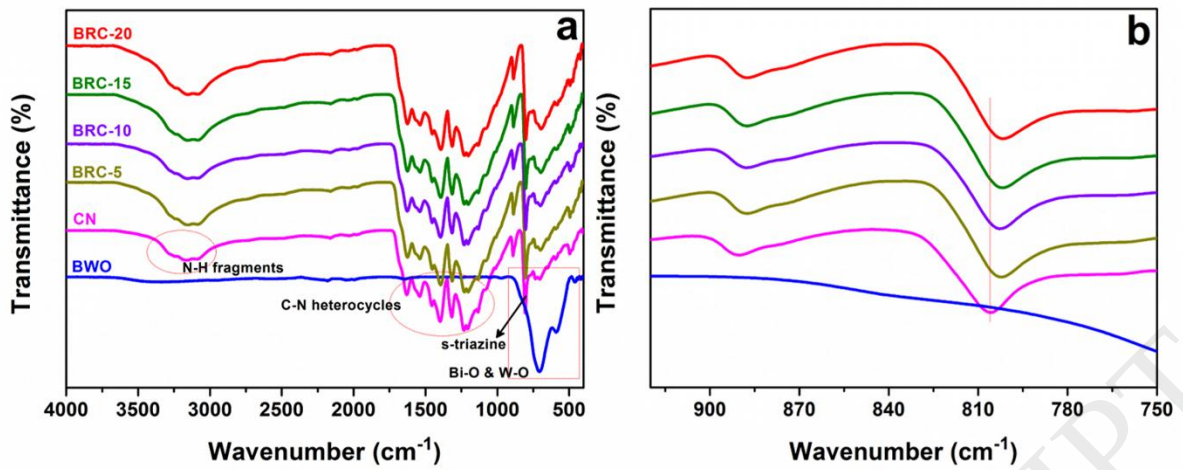

Fig. 6. (a) FT-IR and (b) magnified FT-IR profiles of the prepared CN, BWO, and BWO/RGO/CN heterojunction catalysts.

ACCEPTED MANUSCRIPT

ACCEPTED MANUSCRIPT

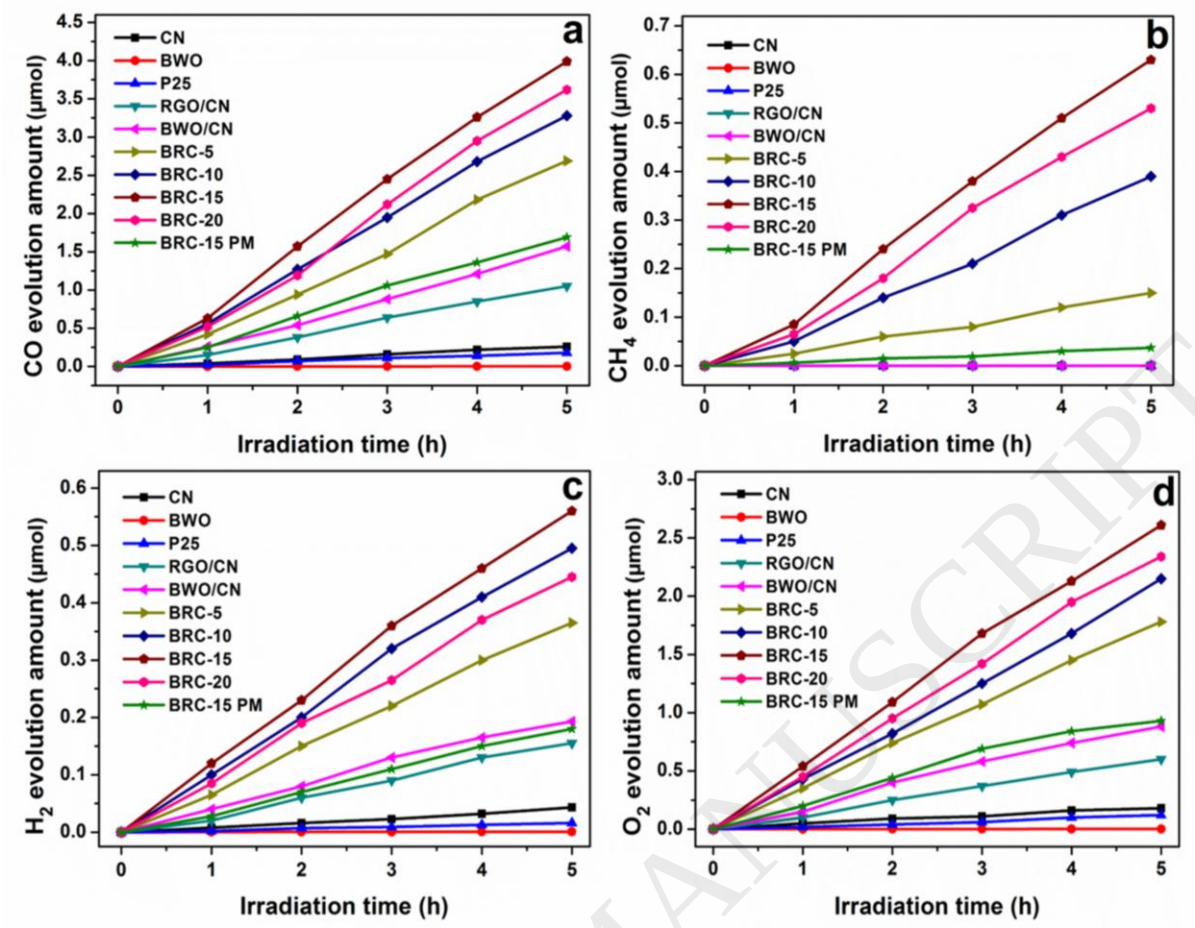

Fig. 7. Time-dependent (a) CO, (b) CH_4, (c) H_2, and (d) O_2 amounts generated over all the synthesized photocatalysts (conditions: 300 W xenon lamp with a UV cut-off filter ($\lambda \geq 420$ nm) as light source and 50 mg catalyst).

ACCEPTED MANUSCRIPT

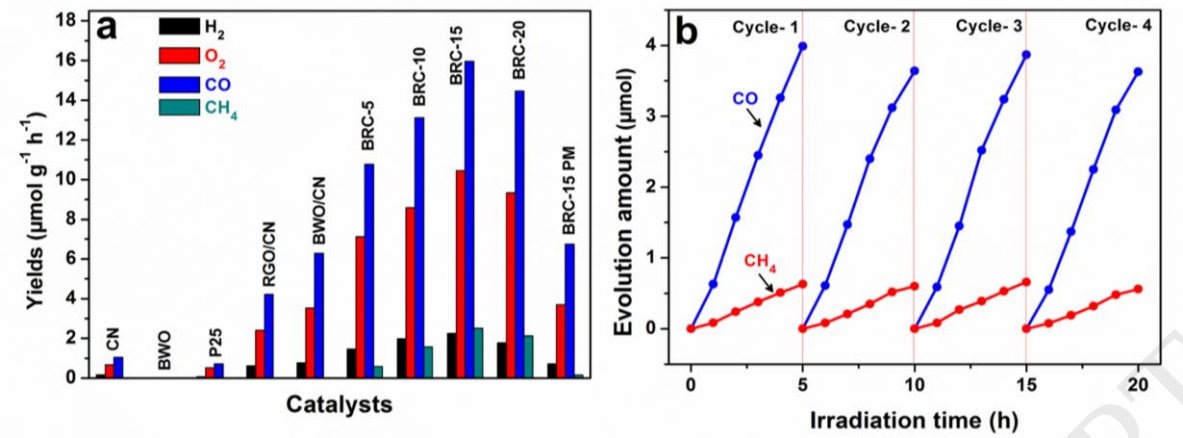

Fig. 8. (a) Comparison of the photocatalytic CO, CH_4, H_2, and O_2 production rates of all the synthesized photocatalysts under visible light illumination for 5 h. (b) Reusability of the optimum BRC-15 catalyst for evolving CO and CH_4 from CO_2 photoreduction over four successive experimental runs.

ACCEPTED MANUSCRIPT

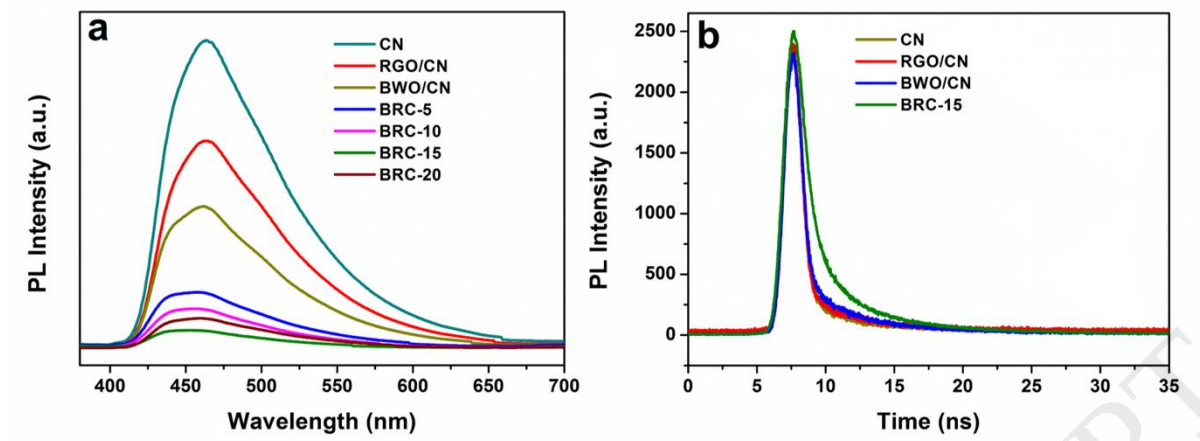

Fig. 9. (a) Steady-state PL spectra of CN, BWO/CN, RGO/CN, and BWO/RGO/CN catalysts. (b) Time-resolved PL profiles of CN, BWO/CN, RGO/CN, and BRC-15 catalysts.

ACCEPTED MANUSCRIPT

ACCEPTED MANUSCRIPT

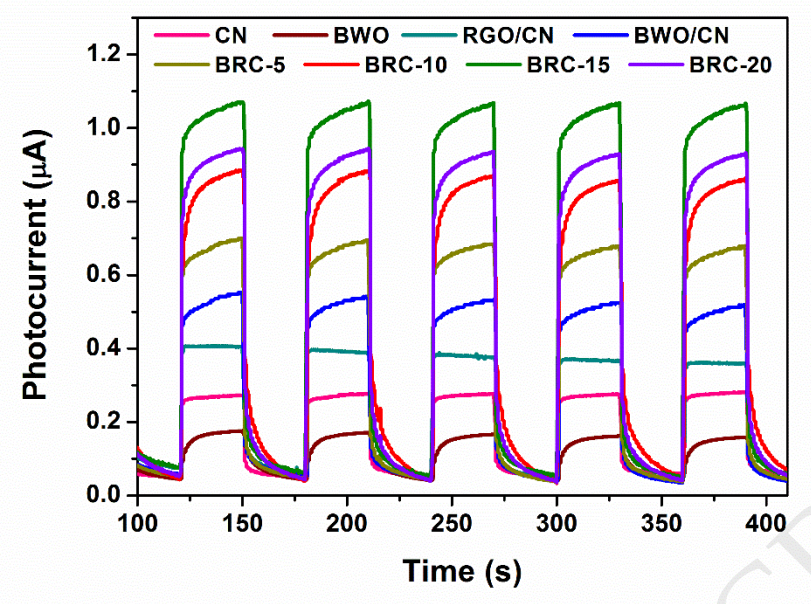

Fig. 10. Photocurrent responses of CN, BWO, BWO/CN, RGO/CN, and BWO/RGO/CN heterojunction catalysts.

ACCEPTED MANUSCRIPT

ACCEPTED MANUSCRIPT

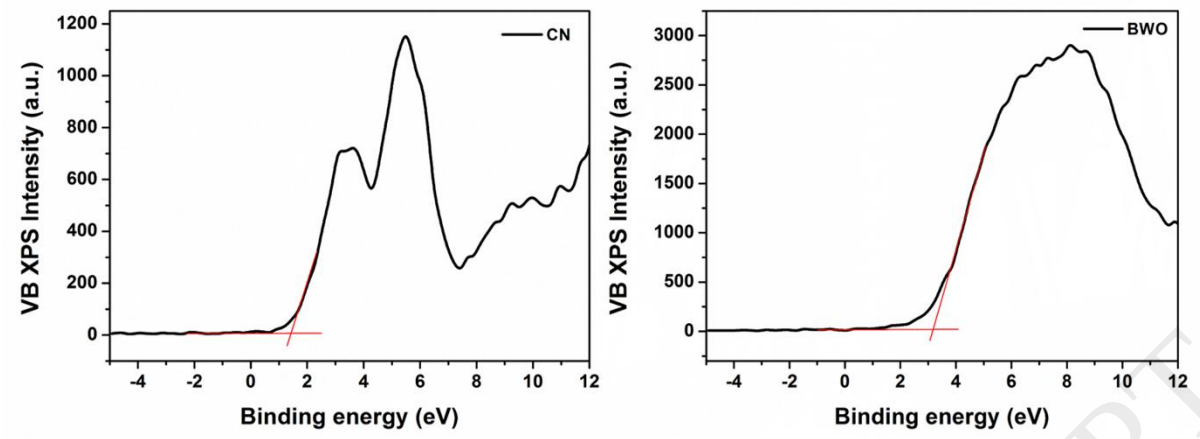

Fig. 11. Valance band XPS profiles of CN and BWO catalysts.

ACCEPTED MANUSCRIPT

ACCEPTED MANUSCRIPT

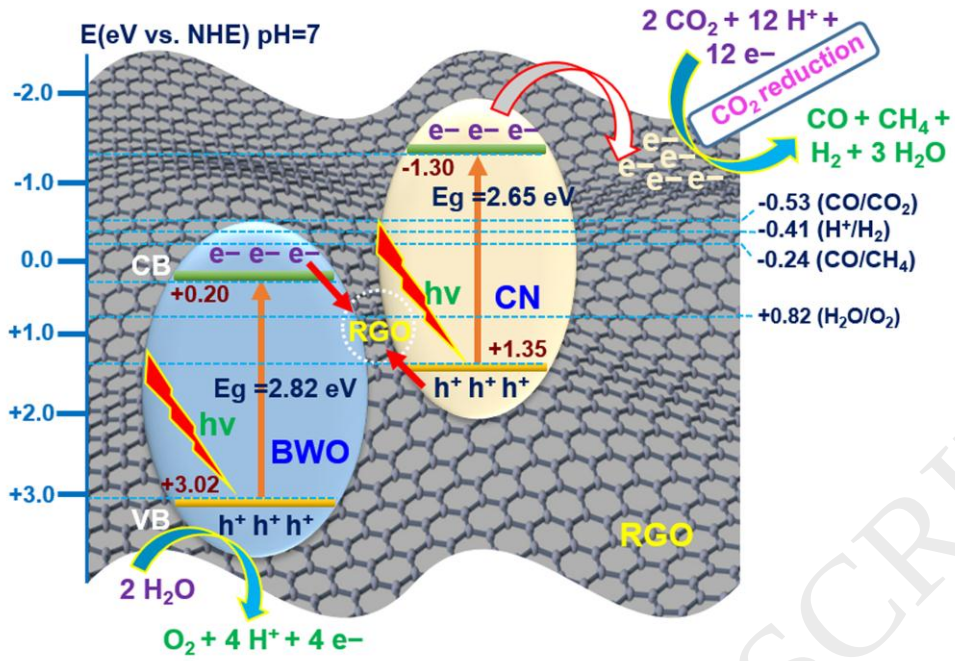

Fig. 12. Schematic illustration of the proposed mechanism for CO_2 photoreduction in the BWO/RGO/CN 2D/2D/2D hybrid heterojunctions.

ACCEPTED MANUSCRIPT